Supporting Information

Sequential p-Type Doping of Polytriphenylamine–SWCNT Composites by Tris(pentafluorophenyl)borane for High-Performance Flexible Thermoelectrics

Riya Martin[a,b], Ramachandran Dheepika[a], Navin Jacob[a,b], Biswapriya Deb[,b,c] and Chakkooth Vijayakumar*[,a,b]*

[a] Chemical Sciences and Technology Division (CSTD), CSIR-National Institute for Interdisciplinary Science and Technology (NIIST), Thiruvananthapuram 695019, Kerala, India.

[b] Academy of Scientific and Innovative Research (AcSIR), Ghaziabad 201002, India.

[c] Centre for Sustainable Energy Technologies (CSET), CSIR-National Institute for Interdisciplinary Science and Technology (NIIST), Thiruvananthapuram 695019, Kerala, India.

E-mail: biswa.niist@csir.res.in (B.D.); vijay.niist@csir.res.in (C.V.)

Experimental Section

Materials and methods

Chemicals: Single-walled carbon nanotubes (SWCNTs; >85% carbon basis, average diameter <3 nm, and average length >5 μm) were purchased from TCI Chemicals. Poly(*N,N′*-bis-4-butylphenyl-*N,N′*-bisphenyl)benzidine (PTPD; M_n > 20,000 g mol^{-1}), anhydrous 1,2-dichlorobenzene (o-DCB, 99%), and tris(pentafluorophenyl)borane (BCF, 95%) were obtained from Sigma-Aldrich. Hexane was procured from Spectrochem. All chemicals were used as received without additional purification.

Preparation of PTPD-SWCNT composite films: The desired amount of SWCNTs was added to a PTPD solution (5 mg/mL) in anhydrous o-DCB and probe-sonicated (VCX-750 Vibra-Cell, Sonics & Materials) for 1 h in a water bath, followed by stirring at room temperature (303 K) for 30 min to ensure uniform dispersion. The composite films were prepared by drop-casting the dispersion onto pre-cleaned glass substrates (16 mm × 4 mm) that had been sequentially cleaned with Extran solution, distilled water, and isopropanol via bath sonication for 15 min in

each solvent. The films were annealed at 120 °C for 30 min to remove residual solvent and improve polymer ordering.

Doping of PTPD-SWCNT composite films: The dopant solution was prepared by dissolving BCF in hexane at 60 °C until complete dissolution. The composite films were immersed in a 2 mg mL^{-1} BCF/hexane solution for 2 min at 60 °C, rinsed with hot hexane to remove excess dopant, and air-dried. The optimized dopant concentration was selected based on the thermoelectric performance trends summarized in Table S2.

Characterization: UV-Vis-NIR absorption spectra (300-2500 nm) were recorded using an Agilent Technologies Cary 5000 spectrophotometer. Raman spectra were acquired on a WiTec Alpha 300 R microscope using a 633 nm excitation laser (7 mW). Film morphology was characterized by scanning electron microscopy (SEM, ZEISS EVO 18) and tapping-mode atomic force microscopy (AFM, Bruker Multimode 8 Nanoscope V). Transmission electron microscopy (TEM) imaging was performed on a JEOL JEM-F200 microscope operating at 200 kV. Elemental composition was determined by SEM equipped with energy-dispersive X-ray spectroscopy (EDX).

For microscopy analysis, SEM samples were annealed at 120 °C to remove residual solvent and sputter-coated with an ultrathin gold layer to ensure conductivity. AFM and TEM samples were prepared by drop-casting composite dispersions onto glass substrates (AFM) or carbon-coated copper grids (TEM), followed by air-drying (AFM) or drying at 30 °C for 24 h (TEM).

Thermal stability was evaluated using a TA Instruments Q50 thermogravimetric analyzer (TGA) with a heating rate of 10 °C min^{-1} from 30 °C to 800 °C under nitrogen. X-ray photoelectron spectroscopy (XPS) was carried out using a PHI 5000 Versa Probe II system equipped with a monochromatic Al Kα X-ray source (hν = 1486.6 eV). Survey and high-resolution spectra were recorded at pass energies of 187.85 eV and 46.95 eV, respectively. Spectra were deconvoluted using MultiPak software, with the C 1s peak at 284.8 eV used for energy calibration and Shirley-type background subtraction.

Surface potential mapping was performed using Kelvin probe force microscopy (KPFM, Bruker Multimode 8 AFM) with a Pt–Ir-coated tip (SCM-PIT-2, Bruker). Hall effect measurements were carried out at room temperature (303 K) using an ECOPIA HMS-3000 system under a 0.54 T magnetic field and 15 mA current in the Van der Pauw configuration. Electrical conductivity and Seebeck coefficient were measured using a Linseis LSR-3 Seebeck system under helium atmosphere. Temperature-dependent thermoelectric measurements were performed from 300 to 450 K. Film thickness was maintained at 2 ± 0.1 μm for all samples,

determined using a Bruker Dektak XT stylus profilometer. Thermal conductivity measurement details are provided in Supplementary Note S1.

Fabrication of Flexible Thermoelectric Generator (TEG): A flexible thermoelectric generator (TEG) comprising seven *p*-type legs was fabricated by drop-casting a PTPD:SWCNT (50 wt%) solution (concentration: 5 mg/mL) onto a 50 μm-thick polyimide substrate, followed by annealing at 120 °C for 30 min. The TE legs were doped by immersion in a 2 mg mL^{-1} BCF/hexane solution for 2 min at 60 °C, rinsed with hot hexane, and air-dried. The legs were connected in series using conductive silver adhesive sheets. The assembled TEG measured 6 cm × 4 cm, with individual legs of 4 mm × 25 mm × 2.5 μm spaced 4 mm apart. Performance testing was conducted using a previously reported home-built setup[1,2], where the temperature gradient (ΔT = 20-100 K) was applied by heating one side and cooling the other with commercial thermoelectric modules. Temperature was monitored using thermocouples attached to both sides of the device. Output voltage and current were recorded using a 2182A nanovoltmeter across variable load resistances, and power output was calculated accordingly.

Artificial Intelligence Tools Declaration: Large language model-based AI tools were used to assist with editorial refinement of manuscript language, reference formatting, and partial drafting of text sections. All scientific data, interpretation, and conclusions are solely the work of the authors, who take full responsibility for the accuracy and integrity of the content presented.

Supplementary Note S1: Thermal Conductivity Measurement and Estimation

Thermal conductivity measurements were performed using a Unitherm 2022 thermal conductance tester (Anter Corporation) following ASTM E-1530 standards. Films were deposited onto 50 mm-diameter, 2 mm-thick PET disks, and the substrate contribution was computationally subtracted during data analysis. The measured value of 0.42 W m^{-1} K^{-1} for PTPD:S50/BCF films represents an apparent thermal conductivity that may underestimate the true value due to:

1. Substrate subtraction uncertainty: For 2 μm films on 2 mm PET substrates, small errors in substrate thermal resistance measurement propagate into large relative errors in extracted film thermal conductivity.
2. Interfacial thermal resistance: The measurement includes polymer-substrate interface resistance, which artificially lowers the apparent film thermal conductivity.
3. Directional considerations: The measurement geometry provides through-plane thermal conductivity, while electrical measurements are predominantly in-plane. Polymer-SWCNT composites can exhibit thermal anisotropy ratios of 3-10×.

Electronic thermal conductivity constraint: The Wiedemann-Franz law provides a lower bound for thermal conductivity: $\kappa_e = L\sigma T = (2.44 \times 10^{-8}\ W\ \Omega\ K^{-2}) \times (15{,}510\ S\ m^{-1}) \times (428\ K) = 1.62\ W\ m^{-1}\ K^{-1}$. Since $\kappa_{total} = \kappa_{electronic} + \kappa_{lattice}$ and $\kappa_{lattice} \geq 0$, the total thermal conductivity must exceed 1.62 W m^{-1} K^{-1}. Recent theoretical work suggests the Lorenz number in heavily doped organic semiconductors may be reduced to $L \approx (0.2\text{-}0.5) \times L_0$, which would lower κ_e to 0.3-0.8 W m^{-1} K^{-1} [3].

Interfacial phonon scattering: The lattice thermal conductivity contribution can be suppressed through: Kapitza resistance at CNT-polymer interfaces (1-10 × 10^{-8} m^2 K W^{-1}), low thermal conductivity of the amorphous polymer matrix ($\kappa_polymer \approx 0.2$ W m^{-1} K^{-1}), and BCF-induced interfacial disorder (evidenced by increased surface roughness from 14.6 to 31.8 nm in AFM).

Electronic and lattice thermal conductivity decomposition: Using Hall effect data (Table S1), at 428 K: $\kappa_e = L_0\sigma T = (2.44 \times 10^{-8}) \times (155{,}100\ S\ m^{-1}) \times (428\ K) \approx 1.62\ W\ m^{-1}\ K^{-1}$. Subtracting from the estimated κ_{total} = 2.0-2.5 W m^{-1} K^{-1} yields $\kappa_L \approx 0.38\text{-}0.88\ W\ m^{-1}\ K^{-1}$, consistent with interfacial phonon scattering suppressing the lattice contribution at CNT-polymer boundaries. BCF-induced surface roughness increase (14.6 → 31.8 nm in AFM) evidences additional interfacial disorder that further scatters phonons without disrupting electrical percolation. The Lorenz number in heavily doped organic semiconductors may deviate from L_0 by up to a factor of 5 (Scheunemann & Kemerink, Phys. Rev. B, 2020), which would lower κ_e to ~0.32 W m^{-1} K^{-1} and represents an additional source of uncertainty. The estimated ZT is: $ZT = PF \times T / \kappa = (190 \times 10^{-6}) \times 428 / 2.2 \approx \mathbf{0.037}$, i.e., ZT ≈ 0.03-0.04 for κ = 2.0-2.5 W m^{-1} K^{-1}.

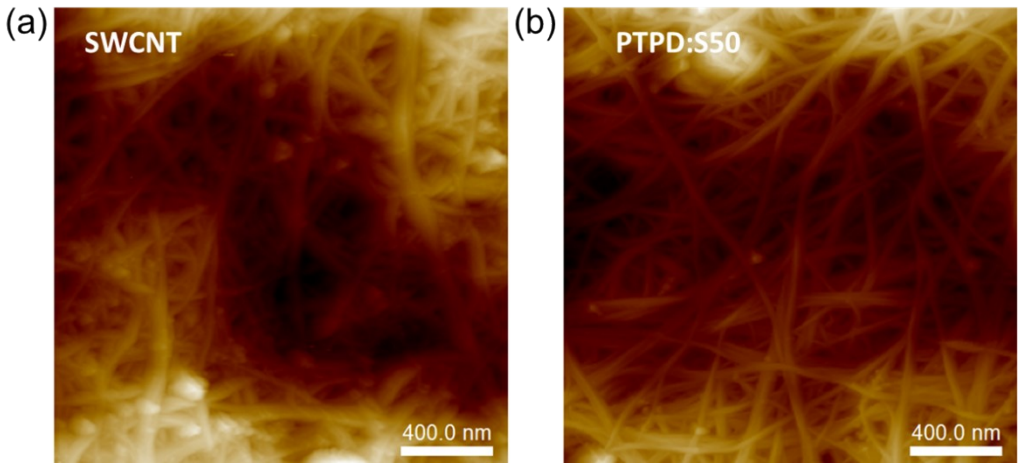

Figure S1. AFM topography images of (a) pristine SWCNT film and (b) PTPD:S50 composite film showing uniform nanotube dispersion.

Table S1. Hall effect measurements of PTPD–SWCNT composite films with varying SWCNT loadings (40-60 wt %) at room temperature (300 K). The data show bulk carrier concentration and mobility extracted from Van der Pauw measurements.

Sample	Bulk carrier concentration (cm^{-3})	Mobility ($cm^2\ V^{-1}\ s^{-1}$)
PTPD:S40	2.08×10^{21}	1.40×10^{-1}
PTPD:S50	8.64×10^{21}	3.02×10^{-1}
PTPD:S60	4.55×10^{21}	2.70×10^{-1}

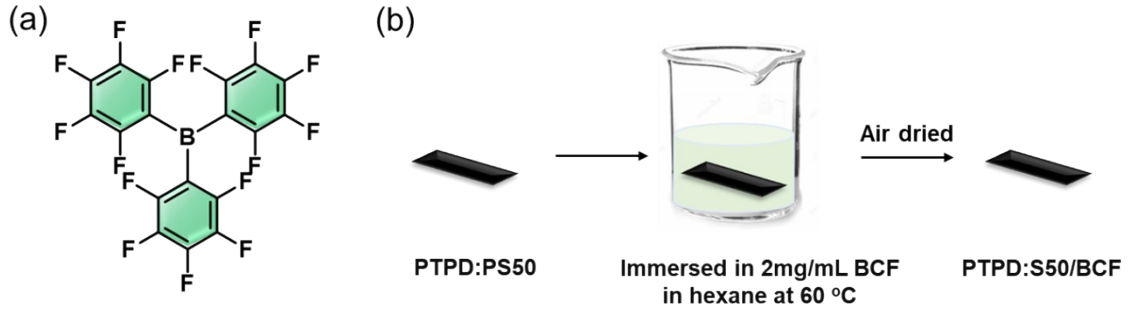

Figure S2. (a) Molecular structure of tris(pentafluorophenyl)borane (BCF). (b) Schematic illustration of the sequential Lewis acid doping process for the PTPD-SWCNT composite film.

Table S2. Thermoelectric parameters of BCF-doped PTPD:S50 composite films at varying dopant concentrations. Electrical conductivity (σ), Seebeck coefficient (S), and power factor ($PF = S^2\sigma$) were measured at room temperature (300 K). The optimal performance was obtained at a BCF concentration of 2 mg mL^{-1}.

Dopant concentration (mg mL^{-1})	σ (S cm^{-1})	S (μV K^{-1})	PF (μW $m^{-1}\ K^{-2}$)
0.5	1923	24	111
1	2001	24	115
2	2208	23	117
4	2257	21.4	104
6	2341	20.1	94

Table S3. Thermoelectric parameters of BCF-doped PTPD:S50 films prepared under three controlled humidity conditions.

Condition	σ (S cm^{-1})	S (μV K^{-1})	PF (μW m^{-1} K^{-2})
Glovebox (RH < 1%)	725	24.9	44.9
Controlled (RH ≈ 30–35%)	1266	23.7	71.0
Ambient (RH ≈ 70–80%)	2201	23.1	117.4

Table S4. Hall-effect characteristics of pristine and BCF-doped PTPD:S50 composite films at room temperature (300 K). Bulk and sheet carrier concentrations and carrier mobilities were determined from Van der Pauw measurements under a 0.54 T magnetic field. A nearly fourfold increase in carrier concentration and ~36 % enhancement in mobility upon BCF doping confirm efficient hole generation *via* the BCF·H_2O Brønsted acid pathway and minor N→B coordination, consistent with XPS, KPFM, and ^{11}B NMR analyses.

Sample	Bulk concentration (cm^{-3})	Sheet concentration (cm^{-2})	Mobility (cm^{-3}V^{-1}s^{-1})
PTPD:S50	8.64E+21	2.51E+18	3.02E-1
PTPD:S50/BCF	3.72E+22	1.15E+19	4.13E-1

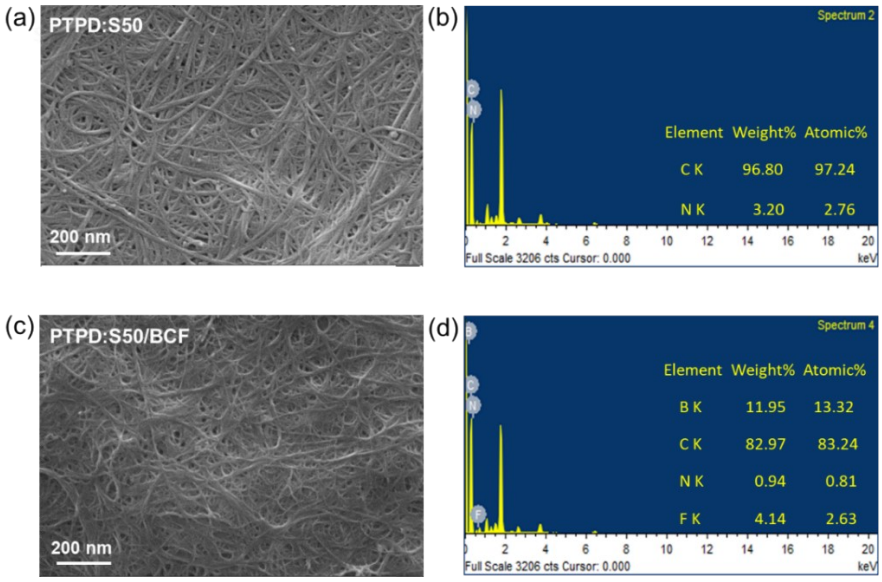

Figure S3. SEM and corresponding EDS spectrum of (a,b) pristine PTPD:S50 composite film and (c,d) BCF-doped PTPD:S50/BCF film. The composite exhibits a uniform, interconnected SWCNT network, while the doped film retains similar morphology, confirming that conductivity enhancement arises from electronic rather than structural changes. EDS spectra show elemental compositions of C, N, B, and F in the composite and BCF doped films.

Composite	Method	σ (S cm^{-1})	S (μV K^{-1})	PF (μW m^{-1} K^{-2})	Ref.
PBDTT-DPP/SWCNT/$FeCl_3$	Immersion	751	42	135	7
PIDF-BT/SWCNT/$AuCl_3$	Immersion	3200	25.84	210	8
PIDF-BT/SWCNT/F4TCNQ	Immersion	5200	15.16	107.6	8
P3Pt/SWCNT	-	5723	23	276.5	9
B-g-C_3N_4/SWCNT	Mixing	2009.8	31.4	198.4	10

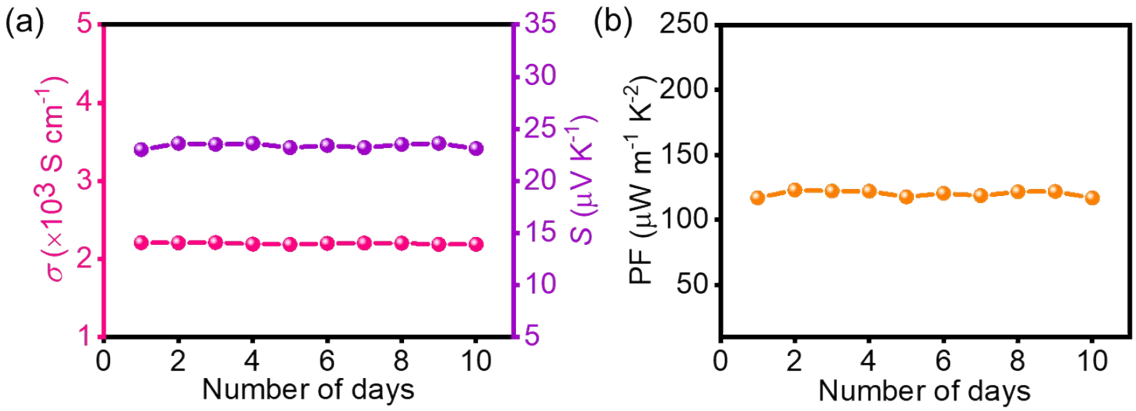

Figure S4. Ambient stability of PTPD:S50/BCF composite films over 10 days (25 ± 2°C, RH 55–65%). Conductivity (σ), Seebeck coefficient (S), and power factor (PF) show minimal degradation (−1.5%, −2.6%, and −7% respectively), confirming doping stability under laboratory conditions.

Table S5. Comparison of thermoelectric (TE) performance parameters of reported doped polymer-SWCNT composites and BCF-doped polymer systems, benchmarked against the PTPD:S50/BCF composite developed in this work. Values of electrical conductivity (σ), Seebeck coefficient (S), and power factor (PF = $S^2\sigma$) are taken from literature at room temperature unless otherwise noted. The PTPD:S50/BCF data are reported at 428 K, representing peak performance. The PTPD:S50/BCF system exhibits one of the highest power factors among solution-processed polymer–nanocarbon hybrids.

P3HT/BCF	Mixing	33	92.5	28.5	11
PCDTFBT/BCF	Mixing	27.9	120	49.6	12
PCDTPT/BCF	Mixing	1.2	147	2.6	12
P3,4EHTV	Mixing	0.34	200	1.47	13
PBDTC2FBT	Mixing	6.4	233	35.1	14
PgBTTT/BCF	Mixing	2180	32	223	15
PBTTT/BCF	Immersion	230	210	140	16
PBTTT/BCF	Mixing	50	400	70	16
PTPD/BCF	Mixing	0.001	104	0.001	17
PTPD/SWCNT/BCF	Immersion	1551	35	190	This work

Table S6. Comparison of the thermoelectric performance of reported PEDOT:PSS/SWCNT-, MXene-, and hybrid composite-based thermoelectric materials and devices in terms of power factor (PF), figure of merit (*ZT*), applied temperature difference (ΔT), and output power (P_o) (devices use single p-type architecture).

Material system	PF ($\mu W\ m^{-1}\ K^{-2}$)	*ZT*	ΔT (K)	P_o (μW)	Ref.
PEDOT:PSS/SWCNT	411	0.10	20	0.39	18
PEDOT:PSS/SWCNT	185	0.10	48	2.60	19
PEDOT:PSS/MXene	155	0.20	-	-	20

PEDOT:PSS/SWCNT/MXene	162	0.25	60	9.50	21
SWCNT/MXene	200	-	117	1.54	22
PTPD/SWCNT/BCF (this work)	190	0.04-0.05	100	0.30	-

References

1 N. Raveendran, T. Ghosh, V. Ignatious, V. Darshan, N. Jacob, B. Deb and C. Vijayakumar, *Mater. Today Energy*, 2023, **34**, 101296.

2 V. Ignatious, N. Raveendran, S. Poovattil, N. Jacob, V. Chakkooth and B. Deb, *Macromol. Mater. & Eng.*, 2022, **307**, 2100916.

3 D. Scheunemann and M. Kemerink, *Phys. Rev. B*, 2020, **101**, 075206.

4 J. Liu, X. Wang, D. Li, N. E. Coates, R. A. Segalman and D. G. Cahill, *Macromol.*, 2015, **48**, 585–591.

5 Y. Zhang, C. Zhu, Y. Chen, L. Wang, X. Huang, L. Zeng and W. Lv, *S&I*, 2024, **50**, 104526.

6 B. Dörling, I. E. Jacobs, I. Brunetti, N. J. Pataki, S. K. Yee, D. Scheunemann, K. Kang, G. Zuo, J. S. Reparaz, T. Mori, M. L. Chabinyc, C. Müller, M. Caironi, M. Kemerink and M. Campoy-Quiles, *Adv. Mater.*, 2026, **38**, e20430.

7 N. Jacob, I. Vijitha, N. Raveendran, R. Dheepika, R. Martin, T. P. Yuvaraj, B. Deb and C. Vijayakumar, *Adv. Mater. Technol.*, 2025, **10**, 2500202.

8 D. E. Choi, J. Im, Y. Ahn, K. Hwang, J. Kim, J. E. Kwon, S. K. Park, H. H. Choi and B.-G. Kim, *Small Struct.*, 2024, **5**, 2300321.

9 L. Chen, Z. Sun, J. Li, M.-T. Lau, J. Sun, D. Zhang, W.-Y. Wong, L. Xu, *Compos. Sci. Technol.* 2024, **256**, 110768.

10 X. Ma, Y. Li, C. Jiang, S. Chen, H. Liu, Y. Zhang, Q. Zhang, F. Du, *ACS Appl. Mater. Interfaces* 2025, 17, 14510.

11 E. H. Suh, J. G. Oh, J. Jung, S. H. Noh, T. S. Lee and J. Jang, *Adv. Energy Mater.*, 2020, **10**, 2002521.

12 E. H. Suh, S. B. Kim, H. S. Yang and J. Jang, *Adv. Funct. Mater.*, 2022, **32**, 2207413.

13 W.-N. Wu, K. Sato, J.-H. Fu, Y.-T. Chan, J.-M. Lin, S.-H. Tung, T. Higashihara and C.-L. Liu, *J. Mater. Chem. A*, 2023, **11**, 17091–17100.

14 H. J. Cheon, T. S. Lee, J. E. Lee, S. B. Kim, E. H. Suh, S.-K. Kwon, Y. J. Jeong, J. Jang and Y.-H. Kim, *Chem. Mater.*, 2023, **35**, 1796–1805.

15 N. Chen, T. Mukhopadhyay, Y. Song, S. Griggs, C. J. Kousseff, I. McCulloch and H. E. Katz, *Adv. Funct. Mater.*, 2024, **34**, 2400469.

16 J. Kim, D. Ju, S. Kim and K. Cho, *Adv. Funct. Mater.*, 2024, **34**, 2309156.

17 W. Lee, H. Kim and Y. Kim, *Adv. Energy and Sustain. Res.*, 2023, **4**, 2300009.

18 L. Zhang, B. Xia, X.-L. Shi, W.-D. Liu, Y. Yang, X. Hou, X. Ye, G. Suo, Z.-G. Chen, *Carbon* 2022, **196**, 718.

19 B. Xia, X.-L. Shi, L. Zhang, J. Luo, W.-Y. Chen, B. Hu, T. Cao, T. Wu, W.-D. Liu, Y. Yang, Q. Liu, Z.-G. Chen, *Chem. Eng. J.* 2024, **486**, 150305.

20 X. Guan, W. Feng, X. Wang, R. Venkatesh, J. Ouyang, ACS *Appl. Mater. Interfaces* 2020, **12**, 13013.

21 S. Zhang, H. Wang, J. Fu, G. Chen, *Energy Mater. Adv.* 2025, **6**, 0143.

22 J. Wei, D. Wu, C. Liu, F. Zhong, G. Cao, B. Li, C. Gao, L. Wang, *Chem. Eng. J.* 2022, **439**, 135706